8 Biological Science

8-1 Structural Basis of the Allosteric Activation of HutP-mediated Anti-termination of Transcription

Bacteria exploit a variety of mechanisms to regulate transcription elongation, in order to control gene expression in response to changes in their environment. Among these, a common path is the modulation of mRNA secondary structures by RNA-binding proteins, either to pause the transcription near the terminator region or to allow synthesis of the full-length transcript [1]. One such anti-terminator protein is HutP, Histidine utilizing Protein, of *Bacillus subtilis*, which is responsible for the regulation of the expression of the *hut* structural genes of this organism in response to changes in the intracellular levels of L-histidine. In the *hut* operon, *hutP* is located just downstream from the promoter, while the five subsequent structural genes, *hutH*, *hutU*, *hutI*, *hutG* and *hutM*, are positioned far downstream from the promoter [2, 3]. In the presence of L-histidine, HutP binds to the nascent *hut* mRNA leader transcript. This allows the anti-terminator to form, thereby preventing the formation of the terminator and permitting transcriptional read through into the *hut* structural genes. In the absence of L-histidine, HutP does not bind to the *hut* mRNA, thus allowing the formation of a stem loop terminator structure within the nucleotide sequence located in between the *hutP* and structural genes.

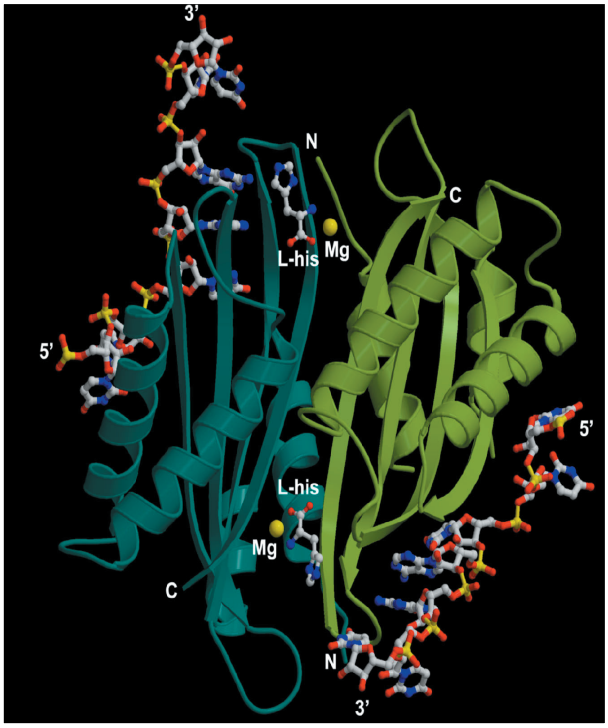

Figure 1
HutP dimer (blue and green) viewed along the pseudo-two-fold axis. The L-histidine and RNA are shown as ball-and-stick models and the Mg^{2+} ions are represented by yellow sphears.

In order to understand the structure of HutP, we solved crystal structure of the HutP, which revealed a novel fold where three dimers are arranged in a 3-fold axis to form a hexamer [4]. We also identified a minimal RNA binding element sufficient for the HutP binding: three UAG trinucleotide motifs, each separated by 4 nucleotides, located just upstream of the terminator, spanning the region between +496 and +515 nucleotides [4]. On the basis of in vitro selections and site-specific mutational analyses, we also identified UAGNNNNUAGNNNNUAG as the recognition motif, in which N indicates any base, and the important chemical groups of the bases for HutP recognition within the core region of the UAG motif [5]. At present, the attenuation/anti-termination protein-RNA complex structures are available for only two proteins, including the full-length TRAP and the amino-terminal

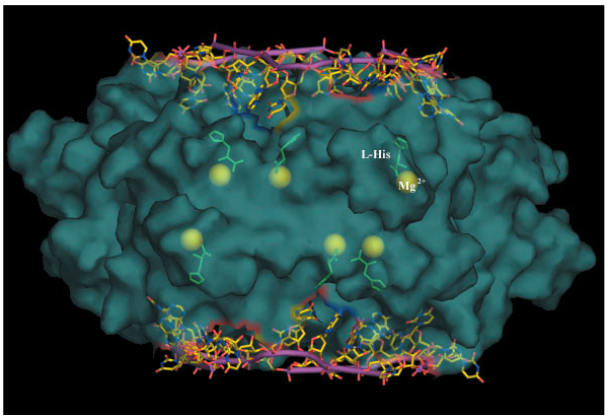

Figure 2
Side view of the molecular surface representation of HutP hexamer. Ball-and-stick models were used for L-histidine and the bound 21-mer RNA. Mg^{2+} are indicated by yellow sphears.

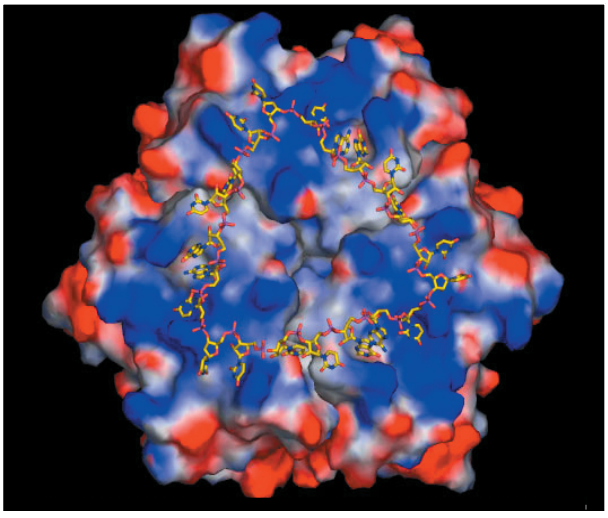

Figure 3
Molecular surface representation of the quaternary complex and the bound RNA shown in a Ball-and-stick model.

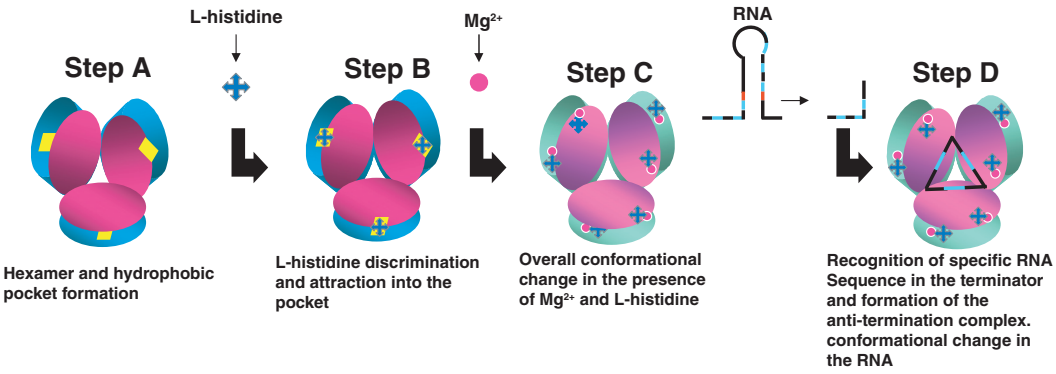

Figure 4
A schematic model proposed for HutP anti-terminator complex formation.

peptide fragment of the LicT. However, the activation of TRAP and their conformational changes before binding to the cognate RNA is remained unknown.

Our recently published study on HutP and their complexes, using AR-NW12A, revealed not only anti-termination complex structure of HutP but also the intermediate structures of HutP to explain allosteric activation of HutP before binding to the cognate RNA [6]. The quaternary complex structure shows how HutP specifically recognizes the conserved sequences within the *hut* mRNA, and reveals the unexpected direct role of the Mg^{2+} ion for mediating the L-histidine-dependent structural rearrangement in the protein (Fig. 1). The overall HutP protein forms the hexamer structure (Figs. 2 & 3). The bound 21-mer RNA was recognized on both the top and bottom surfaces of the cylinder of the HutP in a previously unreported triangular conformation (Fig. 3).

To unravel these structural changes in HutP, we have solved two additional crystal structures (uncomplexed HutP and HutP-L-histidine-Mg^{2+}) and found that the Mg^{2+} ion coordinates with the L-histidine to facilitate an appropriate structural rearrangement before the recognition of its cognate RNA. In considering the various structural and biochemical studies on HutP, we have proposed the model for the structural rearrangement of HutP at each stage (Fig. 4). It appears from these evidences, once HutP has undergone this structural rearrangement, it binds specifically to the RNA sequences within the terminator regions and wraps the terminator/anti-terminator region of hut mRNA around the protein; by this the RNA structure may reorganize and destabilize the terminator structure [6].

T. Kumarevel[1,2], H. Mizuno[3] and P. K. R. Kumar[1] ([1]AIST, [2]RIKEN Harima Inst., [3]NEC Soft. Ltd.)

References

[1] C. Yanofsky, *Annu. Rev. Biochem.*, **70** (2001) 1.
[2] M. Oda, A. Sugishita and K. Furukawa, *J. Bacteriol.*, **170** (1988) 3199.
[3] L. V. Wray, Jr. and S. H. Fisher, *J. Bacteriol.*, **176** (1994) 5466.
[4] T. Kumarevel, Z. Fujimoto, P. Karthe, M. Oda, H. Mizuno and P. K. R. Kumar, *Structure,* **12** (2004) 1269.
[5] T. Kumarevel, S. C. B. Gopinath, S. Nishikawa, H. Mizuno and P. K. R. Kumar, *Nucleic Acids Res.,* **32** (2004) 3904.
[6] T. Kumarevel, H. Mizuno and P. K. R. Kumar, *Nature,* **434** (2005) 183.

8-2 Structural Basis for Ca^{2+}-induced Activation of Human PAD4

PAD (protein-arginine deiminase, protein L-arginine iminohydrolase) is a Ca^{2+}-dependent enzyme that catalyzes the conversion of protein arginine residues to citrulline residues [1]. To date, five types of human PADs 1, 2, 3, 4, and 6 have been characterized by cDNA cloning. PAD4 is the only type of PAD present in the cell nucleus and functions in the citrullination of histones H2A, H3, H4, and nucleophosmin/B23 [2, 3]. PADs and citrullinated proteins are associated with the human diseases such as rheumatoid arthritis (RA). RA is characterized by large numbers of antibodies, directed against citrullinated proteins, produced by the recognition of protein citrulline residues as a major epitope of autoantigens [4]. Recently, a significant association was reported between RA and functional variants of the gene that encoding PAD4 in the Japanese population [5]. To gain insight into the Ca^{2+}-dependent molecular mechanism of protein citrullination by PADs, we determined the crystal structures of Ca^{2+}-free PAD4 and of a Ca^{2+}-bound inactive mutant with and without an artificial substrate for PAD, benzoyl-L-arginine amide (BA), at 2.8 Å, 2.3 Å, and 2.6 Å resolutions, respectively, using the diffraction data collected on NW12A in PF-AR and on BL38B1 and BL45PX in SPring-8 [6].

The PAD4 molecule has an elongated shape like a rubber boot (Fig. 5(a)), an approximate size of 125 x 45 x 50 Å, and is in close contact with another PAD molecule related by a crystallographic 2-fold axis to form a functional dimer (Fig.5 (b)). The polypeptide chain of the molecule is folded into two domains (N- and C-terminal domains). The N-terminal domain consists of the amino acid residues from Met1 to Pro300 and is further divided into two immunoglobulin-like sub-domains (sub-domains 1 and 2). A nuclear localization signal (^{56}PPAKKKST^{63}) is positioned on the molecular surface in the sub-domain 1 and is disordered in all three structures. Functional mutations of the gene encoding PAD4 in the Japanese population for RA are also positioned in sub-domain 1, far from the active site in the C-terminal domain, and are unlikely to affect catalytic function directly.

Asn301 to Pro663 form the C-terminal domain with a

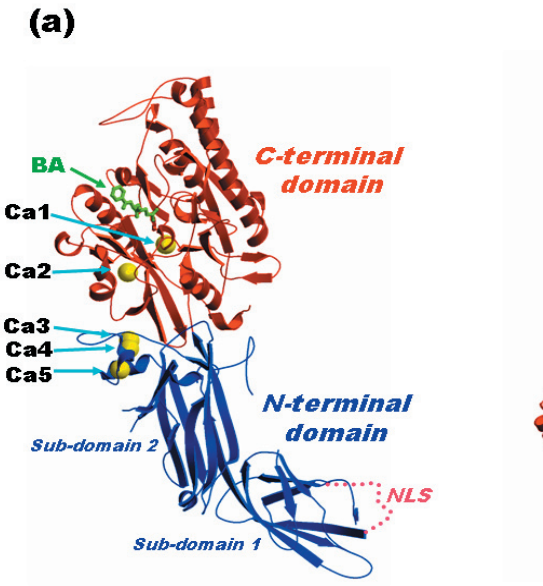

Figure 5
Overall structure of PAD4. (a) Ribbon representation of the monomeric form of Ca^{2+}-bound inactive mutant with an artificial substrate, benzoyl-L-arginine amide (BA). Five Ca^{2+} ions (Ca1, Ca2, Ca3, Ca4, and Ca5) are shown as yellow balls, and BA, as a green ball-and-stick model. N- and C-terminal domains are colored blue and red, respectively. The nuclear localization signal (NLS) region is shown by a dotted line. (b) Ribbon representation of the dimeric form of the substrate complex. A crystallographic 2-fold axis runs vertically at the center of the dimer.

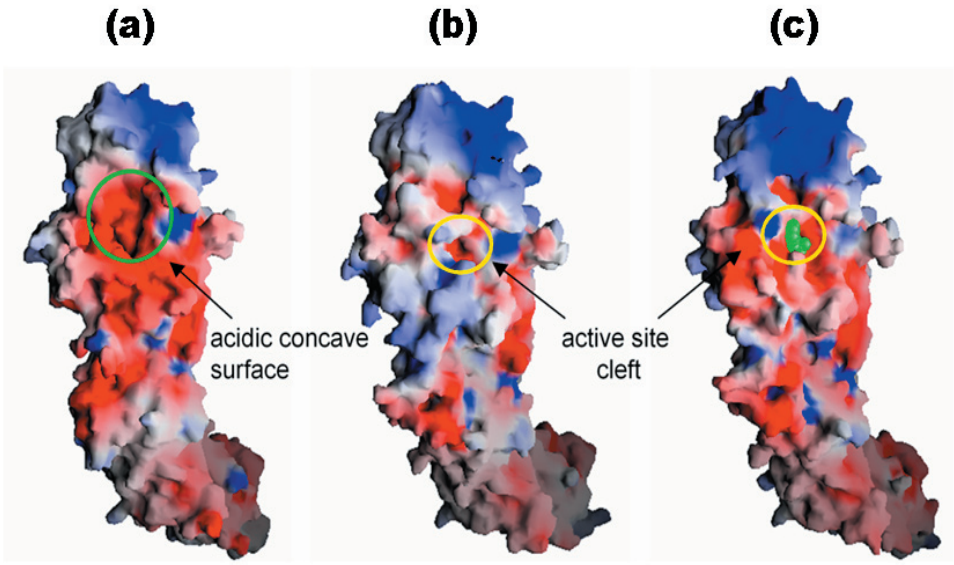

Figure 6
Electrostatic surface potentials of Ca^{2+}-free PAD4 (a), Ca^{2+}-bound inactive mutant (b), and Ca^{2+}-bound inactive mutant with an artificial substrate (c). Surface colors represent the potential from -10 k_BT^{-1} (red) to +10 k_BT^{-1} (blue). The PAD molecule is shown in reverse orientation to that in Fig. 1(a) (seen "through the paper"). The substrate, benzoyl-L-arginine amide, is shown as a green space-filling model. The acidic concave face and the active site cleft are marked by green and yellow circles, respectively.

structure of five ββαβ modules and contain the catalytic residues (Asp350, His471, Asp473, and Cys645). The C-terminal domain of Ca^{2+}-bound mutant PAD4 is almost the same as that of the Ca^{2+}-bound mutant PAD4 with BA, indicating that substrate binding has no effect on the formation of the active site cleft. In contrast, large conformational differences are observed in the C-terminal domains between Ca^{2+}-free PAD4 and Ca^{2+}-bound mutant PAD4. Many disordered portions that form the acidic concave surface at the molecular surface of Ca^{2+}-free PAD4 (Fig. 6(a)) are well ordered in the Ca^{2+}-bound mutant PAD4 and create the active site cleft upon Ca1 and Ca2 binding (Fig.6 (b)). The conformational changes that occur around the active site strongly suggest that binding of Ca1 and Ca2 to the acidic concave surface is crucial for the substrate recognition (Fig.6 (c)). So far, such characteristic Ca^{2+}-induced generation of the active site cleft has not been observed in other Ca^{2+}-dependent enzymes such as calpain [7] and transglutaminase 3 [8], therefore showing that human PAD4 is activated with a novel mechanism by Ca^{2+}.

K. Arita, H. Hashimoto, T. Shimizu, K. Nakashima, M. Yamada and M. Sato (Yokohama City Univ.)

References

[1] E. R. Vossenaar, A. J. W. Zendman, W. J. Venrooij and G. J. M. Pruijn, *BioEssays,* **25** (2003) 1106.
[2] T. Hagiwara, K. Nakashima, H. Hirano, T. Senshu and M. Yamada, *Biochem. Biophys. Res. Commun.,* **290** (2002) 979.
[3] K. Nakashima, T. Hagiwara and M. Yamada, *J. Biol. Chem.,* **277** (2002) 49562.
[4] C. Masson-Bessière, M. Sebbag, E. Girbal-Neuhauser, L. Nogueira, C. Vincent, T. Senshu and G. Serre, *J. Immunol.,* **166** (2001) 4177.
[5] A. Suzuki, R. Yamada, X. Chang, S. Tokuhito, T. Sawada, M. Suzuki, M. Nagasaki, M. Nakayama-Hamada, R. Kawaida, M. Ono, M. Ohtsuki, H. Furukawa, S. Yoshino, M. Yukioka, S. Touma, T. Matsubara, S. Wakitani, R. Teshima, A. Sekine, A. Iida, A. Takahashi, T. Tsunoda, Y. Nakamura and K. Yamamoto, *Nat. Genet.*, **34** (2003) 395.
[6] K. Arita, H. Hashimoto, T. Shimizu, K. Nakashima, M. Yamada and M. Sato, *Nat. Struct. Mol. Biol.,* **11** (2004) 777.
[7] A. Khorchid and M. Ikura, *Nat. Struct. Biol.*, **9** (2002) 239.
[8] B. Ahvazi, H. C. Kim, S. H. Kee, Z. Nemes and P. M. Steinert, *EMBO J.*, **21** (2002) 2055.

8-3 Crystal Structure of the Ankyrin Repeat Domain of Human Ribonuclease L

Interferons (IFNs) are proteins with antiviral, antitumor, and immunomodulatory activities. In the interferon-induced 2-5A system [1], treatment of cells with IFN activates genes encoding several 2',5'-linked oligoadenylate synthetases (OASs) and a single gene encoding ribonuclease L (RNase L). The OASs are activated by binding to dsRNA and generate 5'-phosphorylated, 2',5'-phosphodiester-linked oligoadenylate (2-5A) from ATP. RNase L is activated by binding to 2-5A, changing from an inactive monomer to a catalytically active homodimer. The activated RNase L cleaves viral RNA, and the RNA degradation inhibits protein synthesis and thus inhibits viral replication. The human form of RNase L is a 741-amino acid protein [2]. RNase L consists of three domains, namely the N-terminal ankyrin repeat domain, the protein kinase homology domain, and the C-terminal ribonuclease domain. The N-terminal ankyrin repeat domain is responsible for 2-5A binding, and the C-terminal domain is responsible for catalytic activity. To elucidate the structural basis for 2-5A-dependent dimerization and activation of RNase L, we initiated the structural studies of human RNase L. Recently, we have determined the crystal structure of the N-terminal ankyrin repeat domain (ANK) of human RNase L complexed with 2-5A [3,4].

Crystals of ANK were obtained in the presence of a 2-5A trimer with 5'-monophosphate (Fig. 7). The crystals belong to an orthorhombic space group $P2_12_12_1$ with cell dimensions of a = 63.20 Å, b = 72.83 Å, and c = 82.63 Å. Data collection was preformed at 100 K using the synchrotron radiation of AR-NW12A. The crystal structure of ANK/2-5A complex was determined by the molecular replacement method, and we refined the resulting model to an R-factor of 0.202 (free R-factor of 0.230) at 1.8 Å resolution. The final model consisted of residues 21-305, 220 water molecules, and one 2-5A molecule [3].

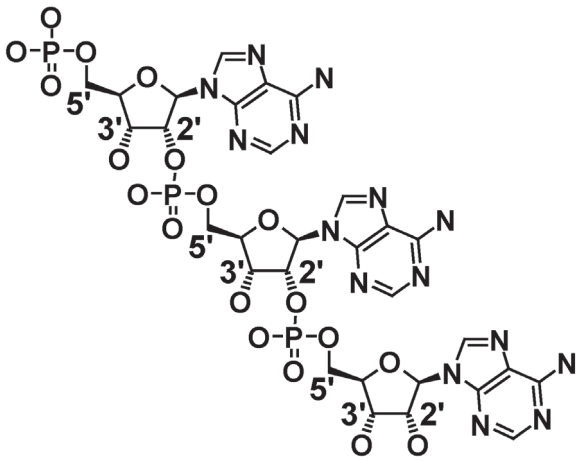

Figure 7
Structure of 5'-monophosphate-type 2-5A used for the present crystal structure analysis.

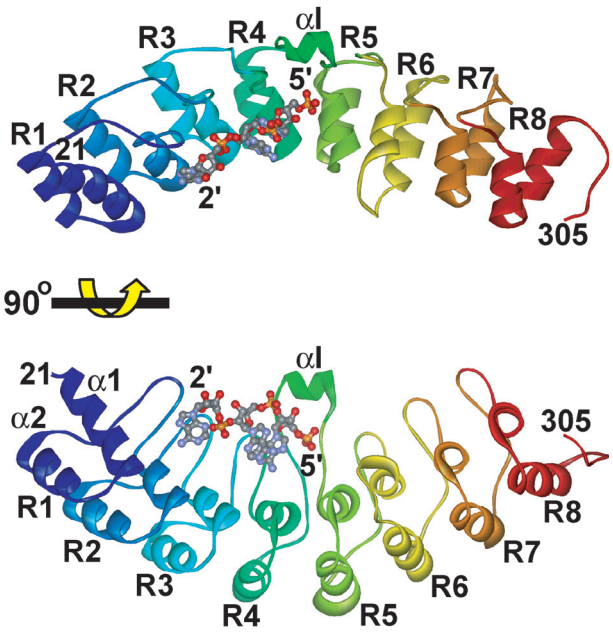

Figure 8
Ribbon representations of the ANK/2-5A complex. The bound 2-5A molecule is shown as a ball-and-stick model.

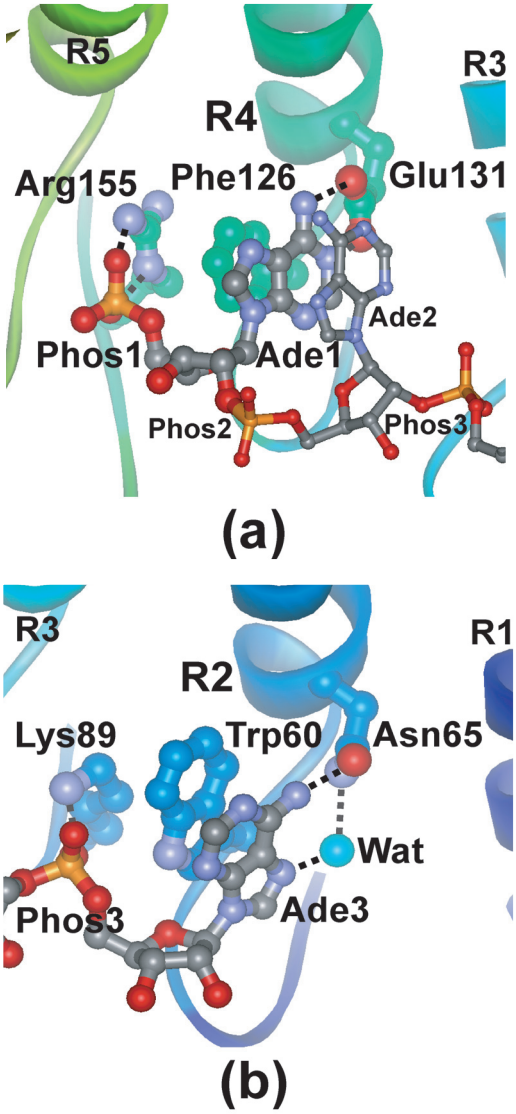

Figure 9
Recognition of the first and third AMP moiety of 2-5A by (a) repeat 4 and (b) repeat 2, respectively, of ANK.

ANK folds into eight ankyrin repeat elements and forms an extended curved structure with a groove running across the long concave surface (Fig. 8). The 2-5A molecule is accommodated in the concavity and directly interacts with ankyrin repeats 2 to 4 (Fig. 9). Interestingly, the 2-5A binding residues in the repeat 4 (R4) and repeat 2 (R2) of ANK are located at the structurally equivalent position of the ankyrin repeat and these residues play a functionally equivalent role. The side chains of Arg155 in R4 and Lys89 in R2 form salt bridge with Phos1 and Phos3, respectively. The side chains of Phe126 in R4 and Trp60 in R2 stack with Ade1 and Ade3, respectively. The side chains of Glu131 in R4 and Asn65 in R2 form hydrogen bonds with Ade1 and Ade3, respectively. Furthermore, a quadruplex (Arg155-Phe126-Ade1-Ade2) and a triplex (Lys89-Trp60-Ade3) of stacking interactions are observed at R4 and R2, respectively.

Because the catalytically active form of RNase L is a potent antiviral and anticellular protein, stable derivatives of 2-5A able to penetrate cell membranes would eventually provide novel therapeutic agents for viral infection and tumor development. The structural basis for 2-5A recognition by ANK is essential for designing stable 2-5As with a high likelihood of activating RNase L.

N. Tanaka, Y. Kusakabe and K. T. Nakamura (Showa Univ.)

References

[1] M. R. Player and P. F. Torrence, *Pharmacol. Ther.*, **78** (1998) 55.
[2] A. Zhou, B. A. Hassel and R. H. Silverman, *Cell,* **72** (1993) 753.
[3] N. Tanaka, M. Nakanishi, Y. Kusakabe, Y. Goto, Y. Kitade and K. T. Nakamura, *EMBO J.,* **23** (2004) 3929.
[4] N. Tanaka, M. Nakanishi, Y. Kusakabe, Y. Goto, Y. Kitade and K. T. Nakamura, *Protein Peptide Lett.,* **12** (2005) 387.

8-4 Crystal Structure of Homolog of Oncoprotein Gankyrin, an Interactor of Rb and CDK4/6

Tumorigenesis is regulated by both oncoproteins and tumor-suppressors which control the G1/S transition during the cell cycle. In this regulatory pathway, one of the key reactions is the phosphorylation of retinoblastoma tumor-suppressor protein (Rb). Rb phosphorylation by cyclin-dependent kinases 4 and 6 (CDK4/6) leads to the release of transcription factor E2F from the Rb-E2F complex. The released E2F triggers activation of a number of genes required for G1/S transition and tumorigenesis. Rb phosphorylation is regulated mainly by ankyrin repeat proteins: gankyrin (Gann ankyrin: Gann means cancer in Japanese) for positive regulation and INK4 (CDK4/6 inhibitor) for negative regulation, in addition to cyclin for activating CDK4/6. Although the cyclin-mediated regulation accounts for the activation of the CDK's intrinsic catalytic activity, the mechanism of *in vivo* Rb phosphorylation at specific residues by CDK is still a great mystery, because Rb contains at least 16 consensus sequences for CDK phosphorylation and the significance of these residues has been demonstrated (Fig. 10a).

Previous studies have revealed that gankyrin-CDK4/6 interaction enhances CDK4/6 phosphorylation activity towards Rb by competing with INK4-CDK4/6 interaction. In contrast to cyclin, gankyrin also interacts with Rb and increases Rb phosphorylation at specific residues i*n vivo*, suggesting that gankyrin has different or additional roles from cyclin for activating CDK. The dual interactions of gankyrin with the substrate (Rb) and enzyme (CDK4/6) are likely to adjust the relative position of those molecules to facilitate site-specific Rb phosphorylation. The INK4-like structure in N-terminal region and LXCXE motif in C-terminal region of gankyrin will provide the relationship of relative positions of gankyrin, CDK4/6, and Rb by superposing the gankyrin with previously reported INK4-CDK4/6 and LXCXE peptide-Rb complex structures (Fig. 10b). Thus, the tertiary structure of gankyrin is a missing piece for elucidating the mechanism of site-specific Rb phosphorylation by CDK4/6.

Recently, we determined the crystal structure of gankyrin homolog, the non-ATPase subunit 6 (Nas6p), refined to 2.3 Å resolution using BL-6A and BL-18B beamlines [1,2] (Fig. 11a). Our results reveal that Nas6p has a concave structure with seven ankyrin repeats. Particularly high conservation between human gankyrin and yeast Nas6p (35% identical and 52% similar over 228 residues) enables us to predict the gankyrin function based on the Nas6p structure (Fig. 11b). The predicted gankyrin-CDK4/6-Rb complex structure model without stereochemical scrambling suggests that gankyrin promotes the correct placement of Rb and CDK4/6. Interestingly, the structurally known region of Rb contains at least two residues (Thr373 and Ser780) for CDK phosphorylation. In this model, Thr373, which is phosphorylated depending on gankyrin overexpression, is close to the active center of CDK4/6 (Fig. 11b). In contrast, Ser780, which is phosphorylated not depending on gankyrin overexpression, is located in the opposite side of the active center of CDK4/6 (Fig. 11b). The crystal structure of Nas6p and our proposed structure model strongly suggests the gankyrin-dependent mechanism for site-specific Rb phosphorylation where gankyrin bridges CDK4/6 and Rb, and makes the active center of Cdk4/6 and the phosphorylation site of Rb face to each other.

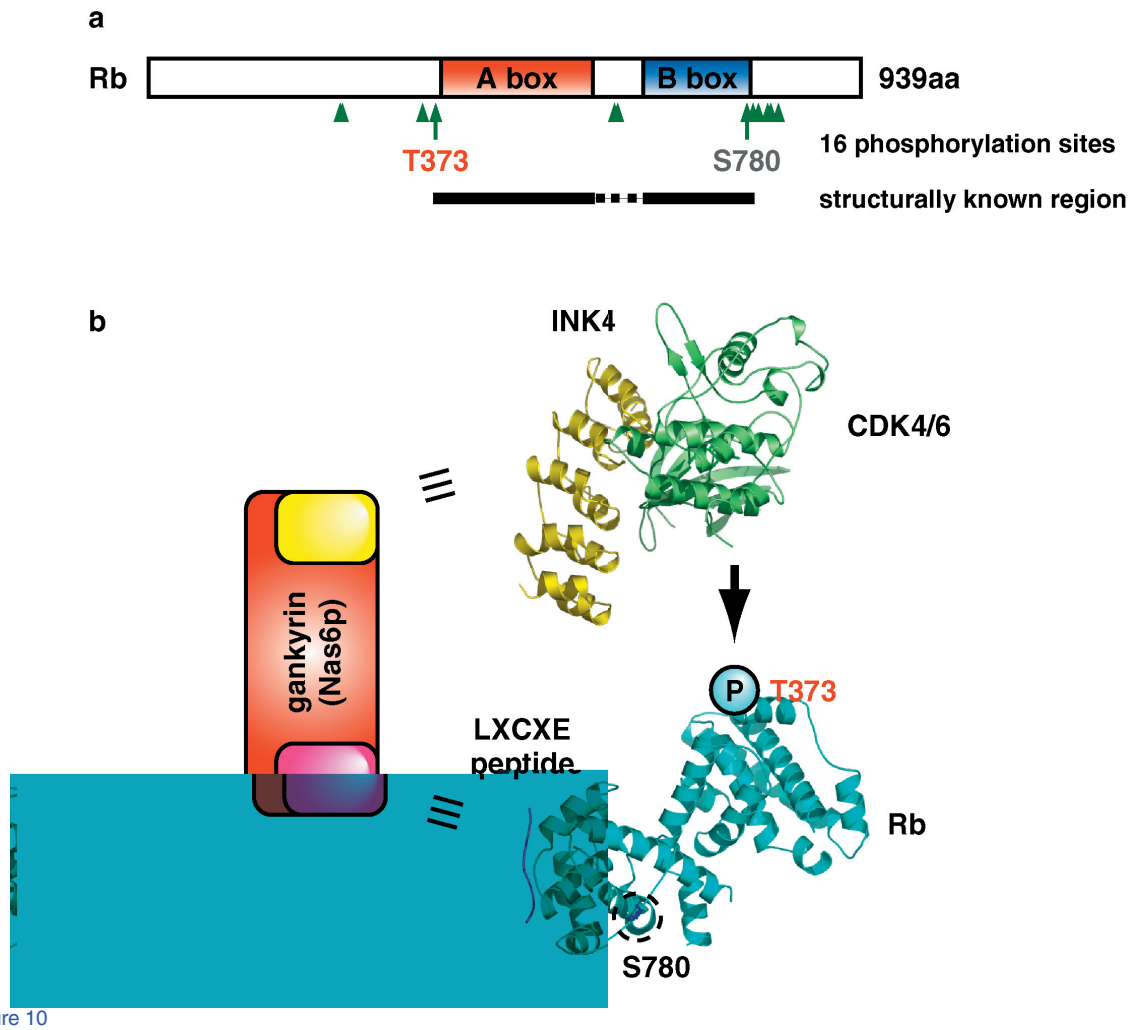

Figure 10
Gankyrin regulates the Rb phosphorylation at specific residues. (a) Domain structure of Rb. Evolutionary conserved regions are shown by A and B boxes. Phosphorylation sites of Rb by CDK4/6 are indicated by arrowheads. Structurally known regions are indicated by black bars. (b) Gankyrin structure will provide the mechanism of specific phosphorylation of Rb by CDK4/6. INK4-like and LXCXE motif regions of gankyrin are shown by yellow and magenta, respectively. Ribbon representations of CDK4/6 (lime), INK4 (yellow), Rb (cyan), and LXCXE peptide (magenta) are shown. Gankyrin-dependent (Thr373) and -independent (Ser780) phosphorylation site of Rb are indicated by "P" and dotted open circle, respectively.

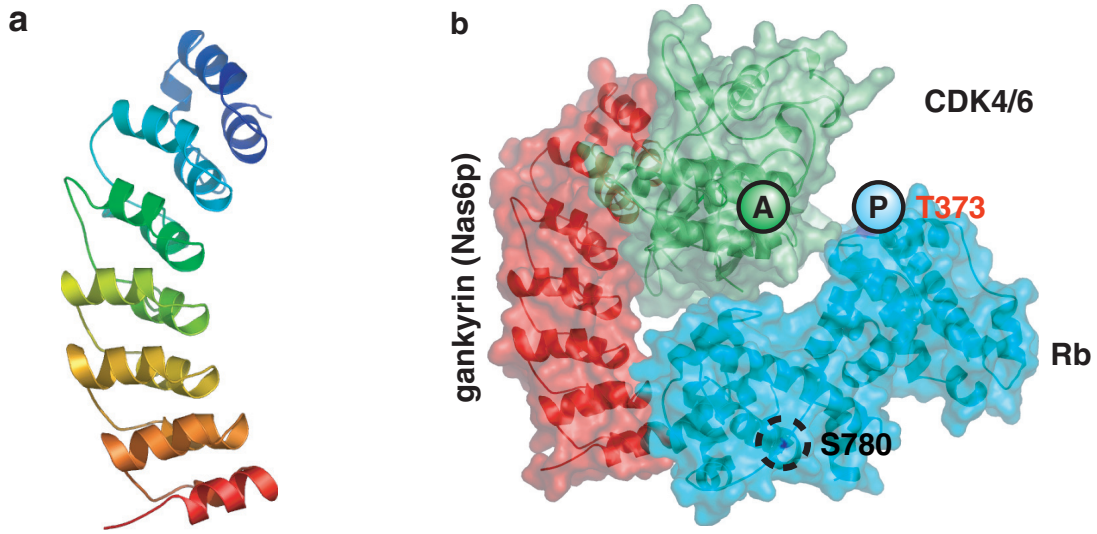

Figure 11
Crystal structure of gankyrin homolog Nas6p. (a) Concave structure with seven ankyrin repeats of Nas6p. (b) The predicted structure model of the gankyrin-CDK4/6-Rb complex. Gankyrin (Nas6p), CDK4/6, Rb are shown by red, green, and cyan, respectively. Active site of CDK4/6 and phosphorylated residues of Rb are shown by A and P/dotted circles, respectively.

B. Padmanabhan[1,3], N. Adachi[1,2,4], K. Kataoka[1,5] and M. Horikoshi[1,2] ([1]ERATO, JST, [2]Univ. of Tokyo, [3]RIKEN GSC, [4]JBIRC, JBIC, [5]GeneCare Res. Inst. Co. Ltd.)

References

[1] N. Adachi, B. Padmanabhan, K. Kataoka, K. Kijima, M. Yamaki, and M. Horikoshi, *Acta Crystallogr. D Biol. Crystallogr.*, **58** (2002) 859.

[2] B. Padmanabhan, N. Adachi, K. Kataoka, and M. Horikoshi, *J. Biol. Chem.*, **279** (2004) 1546.

8-5 Crystal Structure of the Membrane Fusion Protein, MexA, of Bacterial Antibiotic-xenobiotic Exporter

Xenobiotic exporters are ubiquitous to all living organism and protect cells from small noxious compounds. When such transporters are expressed in bacterial cells, they render the cells resistant to many antibiotics. This is a large problem in hospitals. The MexAB-OprM efflux pump of *Pseudomonas aeruginosa*, a hospital pathogen, is one of such transporters that consists of three subunit proteins, MexA, MexB and OprM. Inner membrane spanning MexB recognizes the substrate, OprM forms a long duct extending from periplasmic space to the outer membrane [1], and MexA is supposed to link MexB and OprM. However, precise structure and function of MexA remained to be elucidated.

MexA is a lipoprotein with fatty acid modification at the N-terminal cysteine residue [2]. Removal of the fatty acids by replacing the N-terminal cysteine residue with another amino acid renders MexA totally water-soluble [2]. The MexA crystals were obtained by the hanging-drop vapor diffusion technique at 20°C in the presence of Hepes-Tris buffer pH7.2, glycerol, 2-methyl-2,4-pentandiol, polyethylene glycol 1000 and small amount of Jeffamine-600. Crystals grew to the size of about 0.7 × 0.5 × 0.3 mm^3. The space group was $P2_1$ with cell dimension of a = 130.0 Å, b = 180.3 Å, c = 214.2 Å, β = 107.0°. Diffraction data for structural determination were collected at beam-lines of synchrotron facilities; BL-6A and BL44XU of SPring-8. The MexA structure was determined by a single isomorphous replacement with the anomalous scattering method using the Lu-derivatives [3].

The crystal structure of MexA revealed 68.3% of total amino acid residues. The MexA monomer showed about 130 Å long sickle-like structure consisting of three domains and possibly one additional disordered domain (Fig. 12). MexA had about 50 Å long coiled-coil hairpin structure (α-domain) at one end, then turned about 120° and had linearly aligned two globular domains of about 80 Å long. The globular domain proximal to α-domain consisted of 8 short β-sheets (β-domain), and that distal to α-domain consisted of 7 short β-sheets and one short α-helix (α+β-domain). Disordered domain was

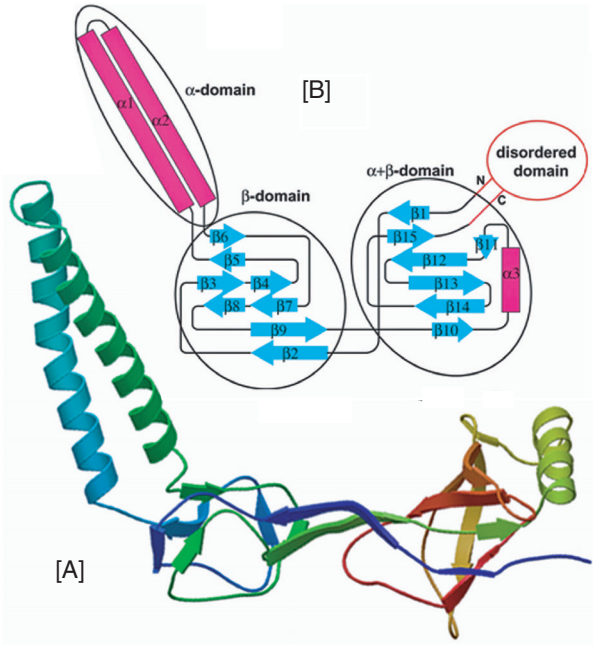

Figure 12
Structural model of the MexA monomer. [A], Ribbon model of MexA based on the crystallographic data showed three domains; α-domain; β-domain and α+β-domain. A density map showed disordered domain adjacent to α+β-domain (not shown). [B], Schematic representation of the MexA structure. Magenta colored rectangle and cyan colored arrow represent α-helix and β-sheet, respectively.

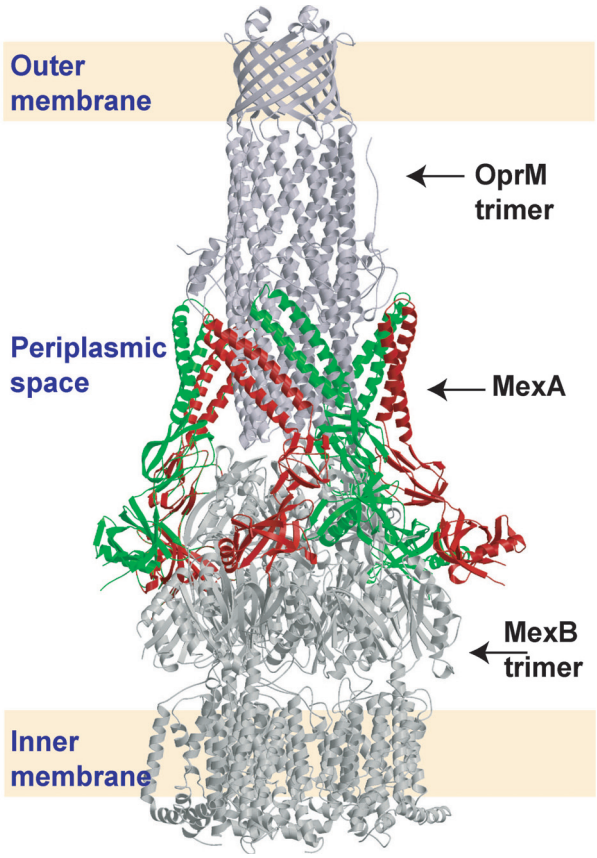

Figure 13
Schematic representation of the MexAB-OprM efflux pump. Figure was drawn based on the crystallographic data of MexA [3], OprM [1], and simulated MexB model based on the AcrB structure of *Escherichia coli* [4]. Three-fold MexA dimers interact with the MexB trimer at the periplasmic end of these subunits. The MexA subunit(s) strengthen this tip-to-tip interaction by clamping them. Number of the MexA subunit is arbitrary.

located adjacent to α+β-domain that consisted of N-terminal 22 residues and C-terminal 95 residues. It is likely that α-domain interacts with the outer membrane protein OprM, and the disordered domain interacts with the inner membrane protein MexB, because the inner membrane-anchoring N-terminal end was located in the disordered domain.

Though the functional role of MexA in the antibiotic export is not clear, it is tempting to speculate the role of MexA as follows. (i) MexA is likely to clamp the MexB and OprM and stabilizes the pump assembly (Fig. 13). (ii) MexA might amplify and transmit the cellular energy conducted by MexB to OprM, and that might trigger opening of tightly closed OprM inlet gate. Based on the structure and possible role of MexA, one can figure how the whole MexAB-OprM efflux pump exports antibiotics. When the substrate molecule comes into the periplasmic space, MexB catches it in the periplasm, then the inner membrane discharges membrane potential and this energy might be transmitted to MexA. MexA transmits the energy to OprM that let the closed inlet of OprM open, easing the flux of the substrate from MexB to the OprM cavity.

T. Nakae[1,2], H. Akama[1], T. Matsuura[3], T. Tsukihara[3], A. Nakagawa[3] ([1]Tokai Univ. School of Medicine, [2]Kitasato Inst., and [3]Osaka Univ. Inst. for Protein Research)

References

[1] H. Akama, M. Kanemaki, M. Yoshimura, T. Tsukihara, T. Kashiwagi, H. Yoneyama, S. Narita, A. Nakagawa and T. Nakae, *J. Biol. Chem.*, **279** (2004) 52816.
[2] H. Yoneyama, H. Maseda, H. Kamiguchi and T. Nakae, *J. Biol. Chem.*, **275** (2000) 4628.
[3] H. Akama, T. Matsuura, S. Kashiwagi, H. Yoneyama, S. Narita, T. Tsukihara, A. Nakagawa and T. Nakae, *J. Biol. Chem.*, **279** (2004) 25939.
[4] S. Murakami, R. Nakashima, E. Yamashita and A. Yamaguchi, *Nature*, **419** (2002) 587.

8-6 Reclassification of Inverting Phosphorylases Based on Structure Determination

Enzymes involved in the formation or cleavage of glycosyl linkages are mainly categorized into Glycoside Hydrolase (GH) or Glycosyl Transferase (GT) class (CAZy website at http://afmb.cnrs-mrs.fr/CAZY/), and each class comprises dozens of families classified on the basis of amino acid sequence similarity. Phosphorylases catalyze cleavage of glycosidic bonds by adding inorganic phosphate to generate glycosyl-phosphates (phosphorolysis). Since the energy of the glycosyl-phosphate bond is not as high as that of a glycosyl-nucleotide, their reactions are reversible. Therefore, phosphorylases can be employed for both the synthesis and degradation of sugar chains. Phosphorylases have been assigned EC numbers of glycosyltransferases (2.4.1.-) according to the apparent

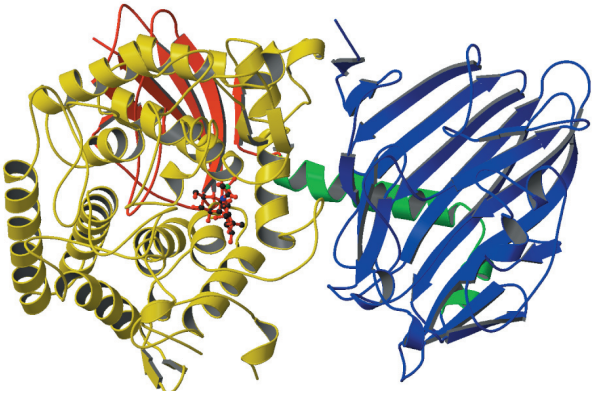

Figure 14
Overall structure of ChBP (N-terminal domain, blue; linker helices, green; α-helical barrel domain, yellow; C-terminal domain, red). The bound GlcNAc molecules are shown as a ball-and-stick model.

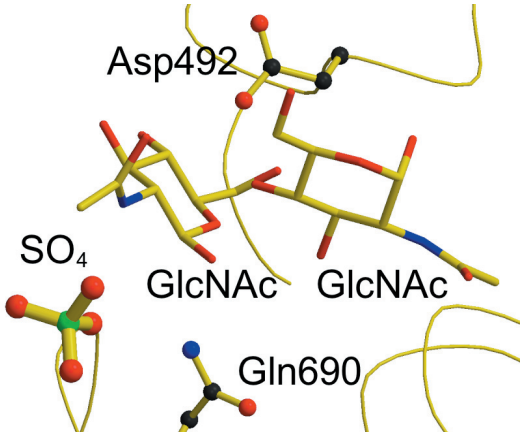

Figure 15
Active site of ChBP.

reaction scheme. However, they occupy a peculiar position in the CAZy database, as they are classified across the GH and GT classes.

Vibrio proteolyticus chitobiose phosphorylase (ChBP) had been belonged to GT-36 family. It catalyzes the phosphorolysis of GlcNAc-β-1,4-GlcNAc (chitobiose) into α-GlcNAc-1-phosphate and GlcNAc with inversion of the anomeric configuration (inverting phosphorolysis). As the first structure of a GT-36 enzyme, we determined the crystal structure of ChBP, using BL-6A and NW12A beamlines [1]. ChBP comprises β sandwich and $(\alpha/\alpha)_6$ barrel domains, constituting a distinct structure from GT folds (Fig. 14). Instead, it shows significant structural similarity with inverting glycoside hydrolases (GH-15 glucoamylase and GH-65 maltose phosphorylase). Moreover, the ternary complex of ChBP with GlcNAc and SO_4 was the first structure of an inverting phosphorylase in a complex with both sugar and anion, and revealed a pseudo-ternary complex structure of enzyme-sugar-phosphate (Fig. 15). Considering the topology of the active site structure, we concluded that the enzymatic phosphorolysis begins with the direct nucleophilic attack by phosphate to the glycosidic bond with the aid of a conserved general acid residue (Asp492), which donates a proton to the glycosidic oxygen atom, and then proceeds through an oxocarbenium cation-like transition state. The

proposed reaction mechanism for the inverting phosphorylase is similar to that for inverting glycoside hydrolases, except that the molecule attacking the C1 atom of the glycoside is a water activated by a general base residue in the inverting GH reaction. The similarities of overall structures and catalytic mechanisms between ChBP and GH enzymes led to a significant reorganization of the CAZy database; family GT-36 was deleted, and then reclassified into a novel GH family, namely GH-94. This type of reclassification, in which a family travels across two functionally distinct classes, was unprecedented. Such structural and functional similarity between inverting glycoside hydrolases and inverting phosphorylases suggests their possible evolutionary relationship.

We have also succeeded in obtaining crystals of cellobiose phosphorylase (CBP), and collected a diffraction data up to 2.1 Å resolution at BL-5A [2]. Among GH-94 enzymes, CBP is the most studied enzyme about substrate specificity and reaction mechanism, and its application for practical oligosaccharide synthesis has been established. The 3D structure of CBP will help technical development on production of new functional oligosaccharides.

M. Hidaka[1,2], Y. Honda[2], M. Kitaoka[2], T. Wakagi[1], H. Shoun[1] and S. Fushinobu[1] ([1]Univ. of Tokyo, [2]Nat. Food Res. Inst.)

References

[1] M. Hidaka, Y. Honda, M. Kitaoka, S. Nirasawa, K. Hayashi, T. Wakagi, H. Shoun and S. Fushinobu, *Structure,* **12** (2004) 937.
[2] M. Hidaka, M. Kitaoka, K. Hayashi, T. Wakagi, H. Shoun and S. Fushinobu, *Acta Cryst. D.*, **60** (2004) 1877.

8-7 Crystal Structure of the Human Sialidase Neu2

Sialidases, or neuraminidases (EC 3.2.1.18), are glycohydrolytic enzymes widely distributed among species from viruses to mammals [1]. Sialidases catalyze the removal of terminal sialic acids from complex carbohydrates, which is considered as the initial step for various biological events such as protein degradation, infection processes, antigenic expression, differentiation, signal transduction or intercellular interactions.

The influenza virus neuraminidase plays an essential role in virus proliferation. When the enveloped virus invades the host cell, a glycoprotein on the virus envelope mediates the attachment and fusion between viral and the host cell membranes [2]. During infection, the virus neuraminidase removes sialic acid from glycoconjugates on the host cell surface, in order to allow the release of newly budding virus particles from the host cell. Several inhibitors such as Tamiflu® (oseltamvir) and RELENZA® (zanamivir) were developed against influenza virus neuraminidase to inhibit the release of virus particles from the host cell [3].

Neu2 is a recently identified human cytosolic sialidase [4], which is highly expressed in skeletal muscle, and at a lower level in liver and brain cells. Although the precise function of Neu2 in human cells is unfortunately unknown, several observations suggest that it might act on ganglioside GM3 leading to the alteration of the cytoskeleton functions. The detailed structural comparison between the virus and human sialidases is expected to provide clues to developing more effective drugs with lower side effects. To elucidate molecular basis of the differences between the diverse sialidases, we determined the crystal structures of human Neu2 in its free form and in complex with an inhibitor, 2-deoxy-2,3-dehydro-*N*-acetyl neuraminic acid (DANA) using the BL-6A and AR-NW12A [5]. These are the first crystal structures of a mammalian sialidase.

The core of the Neu2 enzyme folds as a canonical six-bladed β-propeller with 26 β-strands and five α-helices, similarly to viral and bacterial sialidases. In the Neu2-DANA complex structure, the inhibitor DANA takes a half-chair conformation interacting with ten conserved amino acids of the active site (Fig. 16). An acidic crevice at the center of the β-propeller forms an activating core for the enzymatic catalysis, while the basic residues at the mouth of the crevice coordinate substrates.

The interaction between Neu2 and DANA shows similarities with bacterial and viral counterparts but also exhibits significant differences in the active site arrangement and dynamic nature of the loops containing residues responsible for catalysis and substrate recognition. Two disordered loops on the top side of the apo form Neu2 become visible upon binding of DANA; one loop contains Glu^{111} important for the substrate binding, and the other loop includes Asp^{46} for the catalysis (Fig. 16). Soaking the apo form crystals with monosaccharide such

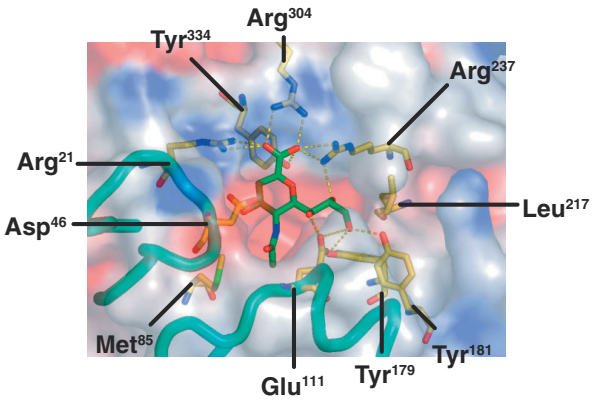

Figure 16
Neu2-DANA interactions. Molecular surface representation of Neu2 active site showing residues involved in DANA coordination. *Dotted yellow lines* indicate interactions between Neu2 and the inhibitor. Neu2 is represented as a *molecular surface* colored according to the electrostatic potential, where *blue* and *red* surfaces indicate areas of positive and negative potential, respectively, over the range from 10 to -10 k_BT. DANA is represented as a *stick* model. The helices α1 and α2 are represented as a *tube* model. Residues involved in the coordination of the ligand are labeled.

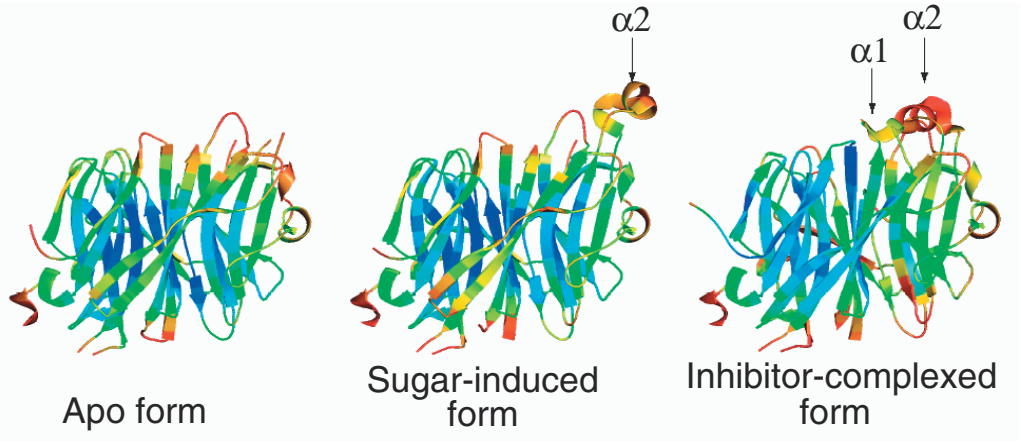

Figure 17
B-factor values of Neu2. Averaged *B*-factor of Neu2 apo form, sugar-induced form and Neu2-DANA complex, represented as a ribbon model. *Red* and *blue* represent high and low *B*-factors respectively. Helices α1 and α2 are indicated by arrows.

as galactose, glucose, or maltose orders the former loop into α2 (Fig. 17), illustrating a plausible two-step model for a dynamic in the substrate recognition. These structures would provide an insight for designing better drugs against viral and bacterial sialidases with no affinities against human counterparts.

L. M. G. Chavas[1], C. Tringali[2], P. Fusi[3], B. Venerando[2], G. Tettamanti[2], R. Kato[1], E. Monti[4] and S. Wakatsuki[1] ([1]KEK-PF, [2]Univ. of Milano, [3]Univ. of Milano-Bicocca, [4]Univ. of Brescia)

References:

[1] M. Saito and R. K. Yu, *Biology of the Sialic Acids, Plenum Press, New York* (1995) 261.
[2] P.M. Colman and M. C. Lawrence, *Nat. Rev. Mol. Cell Biol.*, **4** (2003) 309.
[3] M. V. Itzstein, W. -Y. Wu, G. B. Kok, M. S. Pegg, J. C. Dyason, B. Jin, T. V. Phan, M. L. Smythe, H. F. White, S. W. Woods, R. C. Bethell, V. J. Hotham, J. M. Cameron and C. R. Penn, *Nature*, **363** (1993) 418.
[4] E. Monti, A. Preti, E. Rossi, A. Ballabio and G. Borsani, *Genomics*, **57** (1999) 137.
[5] L. M. G. Chavas, C. Tringali, P. Fusi, B. Venerando, G. Tettamanti, R. Kato, E. Monti and S. Wakatsuki, *J. Biol. Chem.*, **280** (2005) 469.

8-8 X-ray Structures of Non-coding DNA; DNA Octaplex and its Split Quadruplexes Suggesting a Folding Mechanism of Eight Repetitive Sequences for Polymorphism Formation

Recent human genome projects have revealed that the content of coding regions are only a few percent (~1.5%), whereas the huge amounts of repetitive sequences exist in the remaining non-coding regions [1]. Because these repeats sometimes cause diseases, they must have some biological functions with specific structures. However, our knowledge is still limited to few cases. For comprehensive understanding of the controlling systems of these biological phenomena, the non-coding regions should be intensively and extensively studied. A VNTR (variable number of tandem repeats) region immediately adjacent to the human pseudoautosomal telomere [2] shows a high degree of length polymorphism. In this region, the G-rich sequence d(ccGA[G]$_4$Agg) is repeated eight times. To reveal its structural versatility, X-ray analyses of DNA fragments with a related sequence GCGA[G]$_1$AGC (hereafter G1) have been performed using PF beamline BL-18B.

Two different structures have been obtained from G1-lowK and G1-highK crystals prepared at relatively low and high potassium concentrations, respectively (both in the physiological conditions). In both crystal structures, the two adjacent G1 fragments form a base-intercalated duplex, different from the Watson-Crick base-paired duplexes. Between the two sheared-type G_3:A_6* and A_6:G_3* pairs, the central A_4 and G_5 bases are intercalated between G_3 and G_5*, and between G_5* and A_4*, respectively, so that the four bases, A_4, G_5*, G_5 and A_4 are stacked on each other (note the numbering systems of nucleotide residues in Fig. 18).

At low K^+ concentration, the four base-intercalated duplexes [3,4,5] are assembled to form an octaplex [6,7] (Fig. 18). This is the largest multiplex found in nucleic acid crystals so far. In the central part, the eight G_5 residues form two G-quartets, which are stacked on each other. At the center of this *I*-motif of double G-quartets, a potassium cation is bound to stabilize the octaplex formation. At the high K^+ concentration, however, the octaplex is split into just two halves of quadruplexes (Fig. 18). In each half, a potassium cation is bound on the split surface. These two potassium cations separate the split quadruplexes at a distance of 11.5 Å.

The high similarity between the two structures allows us to speculate that at least the two structural states equilibrate in solution depending on potassium concentration. Firstly, two DNA fragments aligned in an anti-parallel fashion are associated to form a base-intercalated duplex, and then two duplexes are assembled to form a quadruplex. Finally, two quadruplexes are further associated to complete an octaplex. These structural features of the sequence d(gcGA[G]$_1$Agc) could be applied to those

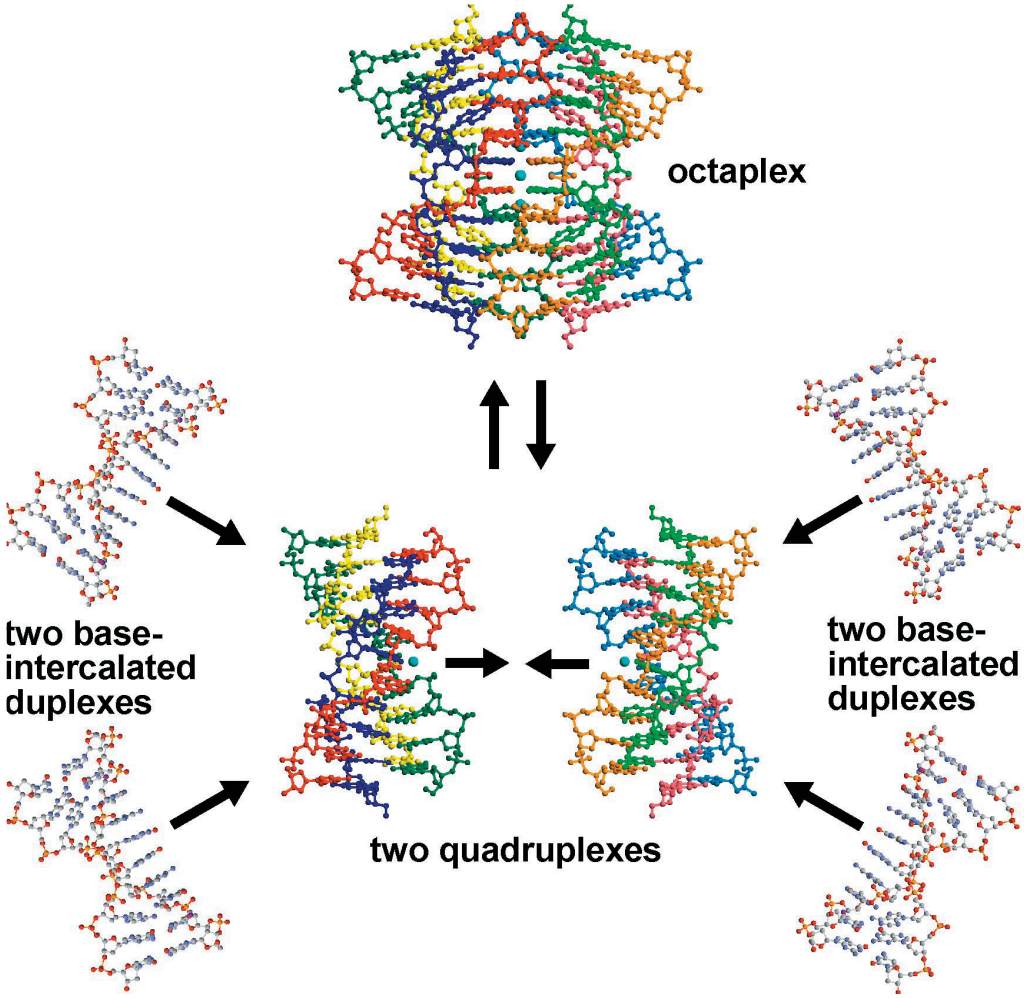

Figure 18
The octaplex formation of d(GCGA[G]$_1$AGC)$_8$. Two DNA fragments are aligned in an anti-parallel fashion and associate to form a base-intercalated duplex, and then the two duplexes are associated to form a quadruplex through potassium-cation mediation. Finally, the two quadruplexes assemble to make an octaplex by releasing some potassium cations.

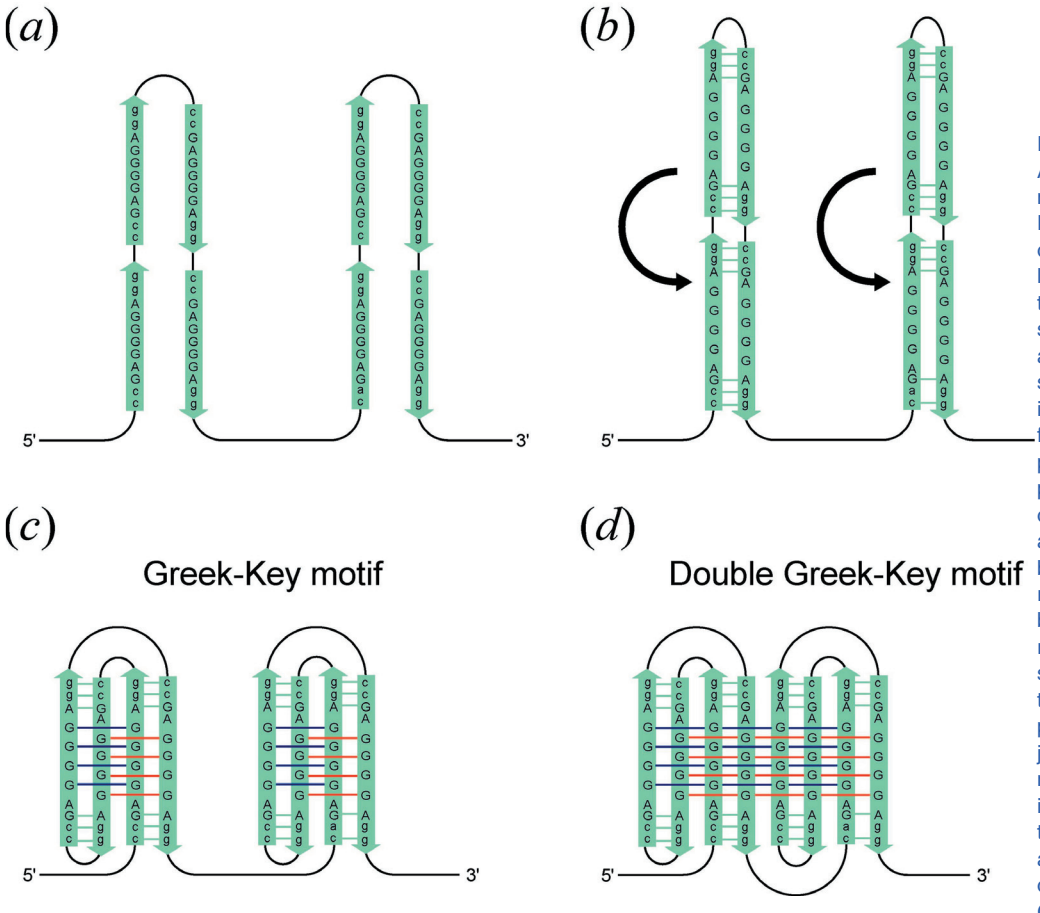

Figure 19
A proposed folding mechanism of a non-coding DNA with eight repeats of d(ccGA[G]$_4$Agg). (*a*) A long chain is folded at the two linkers between the second and third repeats and between the sixth and seventh repeats. (*b*) Base-intercalated duplexes are formed between the anti-parallel strands. (*c*) The two parts are further folded; one is between the first and second repeats and between the third and fourth repeats, and the other is between the fifth and sixth repeats and between the seventh and eighth repeats, to form a quadruplex in each part. This folding pattern is just similar to a Greek-key motif, which is well known in protein folding. (*d*) Finally the two quadruplexes are associated to form an octaplex with a double Greek-key motif.

of the eight repeats of the sequence d(ccGA[G]$_4$Agg) found in the above-described VNTR (Fig. 19). To form an octaplex in local, the folding process is similar to the manner of double Greek-key motifs, as found in protein folding. Such a packaging of the repetitive sequences might induce slippage of the repeats during DNA replication, increasing or decreasing the number of repeats depending on whether slippage occurs on the growing or on the template strand. To confirm the validity of the above hypotheses, more extensive and intensive investigations are required. In addition, it is necessary to reveal the structures of longer octaplexes with *I*-motif of G-quartets.

A. Takenaka (Tokyo Inst. Tech.)

References

[1] International Human Genome Sequencing Consortium, *Nature*, **409** (2001) 860.
[2] C. F. Inglehearn and H. J. Cooke, *Nucleic Acids Res.*, **18** (1990) 471.
[3] T. Sunami, J. Kondo, I. Hirao, K. Watanabe, K. Miura and A. Takénaka, *Acta Crystallogr. D,* **60** (2004) 90.
[4] T. Sunami, J. Kondo, I. Hirao, K. Watanabe, K. Miura and A. Takénaka, *Acta Crystallogr. D,* **60** (2004), 422.
[5] J. Kondo, U. Umeda, K. Fujita, T. Sunami and A. Takénaka, *J. Synchrotron Rad.,* **11** (2004) 117.
[6] J. Kondo, W. Adachi, S. Umeda, T. Sunami and A. Takénaka, *Nucleic Acids Res.*, **32** (2004) 2541.
[7] J. Kondo and A. Takénaka, *J. Crystallogr. Soc. Jpn.*, **46** (2004), 345.

8-9 Crystal Structure of the Terminal Oxygenase Component of Biphenyl Dioxygenase Derived from *Rhodococcus* sp. Strain RHA1

Polychlorinated biphenyls (PCBs) are widely distributed toxic and carcinogenic environmental pollutants. Because of their chemical stability, PCBs are significantly recalcitrant to biodegradation and have accumulated in the tissues of fish, birds and other wildlife. The accumulation of PCBs has even been observed in human bodies. In 1973, Ahmed and Focht discovered a bacterium that can degrade PCBs [1]. Since then some PCB-degrading bacteria have been isolated, and studies on bioremediation with these bacteria have been ongoing. It has turned out, however, that bioremediation is difficult because of the narrow substrate specificity of the PCB-degrading enzymes in the bacteria. Understanding the mechanism of the substrate specificity of these enzymes has, therefore, been one of the most important issues in this field. In particular, the substrate specificity of the first enzyme in the degradation pathway, biphenyl dioxygenase (BDO), is the most important among them. In order to understand the mechanism of the BDO's substrate specificity, we have attempted to solve the crystal structure of BphA1A2, a terminal oxygenase component of BDO. Here, we present the crystal structures of BphA1A2 in substrate-free and complex forms at 2.2Å and 2.6Å resolutions, respectively [2]. The BphA1A2 was derived from the *Rhodococcus* sp. strain RHA1, which is one of the strongest PCB degraders ever found [3-5]. The data collection on BphA1A2 were performed at BL-6A. The crystal structure was determined by the molecular replacement method using the structure of naphthalene dioxygenase as a search model.

BphA1A2, a $\alpha_3\beta_3$ type hetero-hexamer, has a mushroom shape (Fig. 20). The stem and the cap in the mushroom consist of the β_3 and the α_3 subunits, respectively. The active site of the enzyme is located in the α subunit and contains a none-heme iron, which is coordinated by His224, His230 and Asp378. The substrate is located above the none-heme iron (Fig. 21). It is of note that the substrate-binding pocket of the substrate-free form is too small to accommodate the biphenyl molecule. Conformational changes upon substrate binding enlarge the substrate-binding pocket to accommodate the substrate.

The analysis of the present crystal structures with the biochemical data obtained to date on the related BDOs

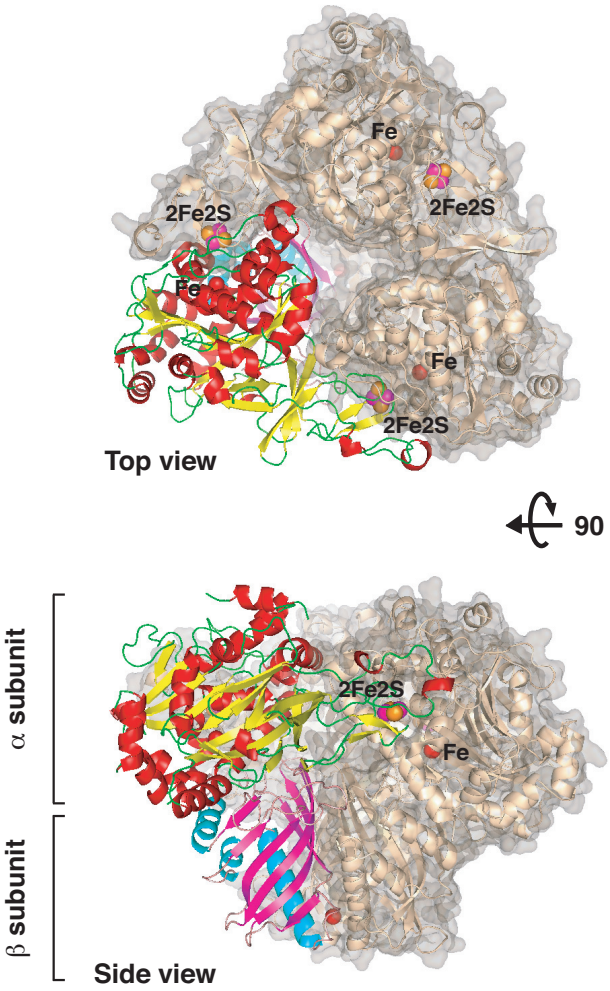

Figure 20
The overall structure of BphA1A2. One protomer (the $\alpha\beta$ complex) is shown in ribbon model. The other part of the molecule are shown in ribbon model with surface representation. The none-heme irons and the [2Fe-2S] Rieske clusters are labeled. Electrons from the ferredoxin component of BphA are accepted with the Rieske cluster, transferred to the none-heme iron, and used for the catalytic reaction.

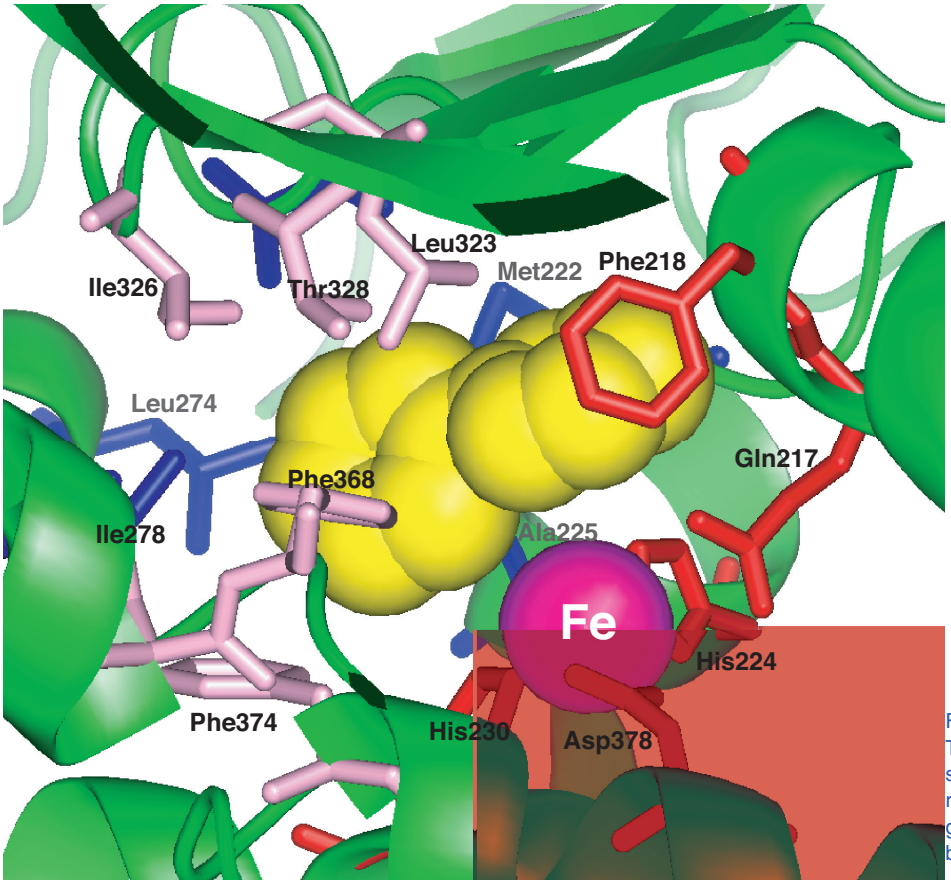

Figure 21
The active site of BphA1A2. The substrate is shown in yellow. The residues in the first, second and third groups are shown in red, pink and blue, respectively.

suggests that residues in the substrate-binding pocket can be roughly divided into three groups in terms of their functions. Residues in the first group (shown in red in Fig. 21) are located around the Fe ion, and are important in forming the chamber for the catalytic reaction. The residues belonging to the second group (shown in pink in Fig. 21) are likely to control the orientation/conformation of the bound substrate. Mutations on these residues tend to alter the substrate specificity and regiospecificity of the enzyme. Residues of the third group (shown in blue in Fig. 21) are less conserved among the related enzymes, and likely to make significant conformational changes upon substrate binding, as described above.

Y. Furusawa[1, 2], V. Nagarajan[3], M. Tanokura[2], E. Masai[3], M. Fukuda[3] and T. Senda[1] ([1]BIRC- AIST, [2]Univ. Tokyo, [3]Nagaoka Univ. Tech.)

References

[1] M. Ahmed and D. D. Focht, *Can. J. Microbiol.*, **19** (1973) 47.
[2] Y. Furusawa, V. Nagarajan, M. Tanokura, E. Masai, M. Fukuda and T. Senda, *J. Mol. Biol.*, **342** (2004) 1041.
[3] M. Seto, K. Kimbara, M. Shimura, T. Hatta, M. Fukuda and K. Yano, *Appl. Environ. Microbiol.*, **61** (1995) 3353.
[4] M. Seto, E. Masai, M. Ida, T. Hatta, Z. Kimbara, M. Fukuda and K. Yano, *Appl. Environ. Microbiol.*, **61** (1995) 4510.
[5] E. Masai, A. Yamada, J. M. Healy, T. Hatta, K. Kimbara, M. Fukuda and K. Yano, *Appl. Environ. Microbiol.*, **61** (1995) 2079.

8-10 Role of the Helical Protrusion in the Conformational Change and Molecular Chaperone Activity of the Archaeal Group II Chaperonin

Protein folding is assisted by a number of molecular chaperones *in vivo*. The chaperonins, a ubiquitous class of molecular chaperones, form double-ring complexes that mediate the folding of nascent and denatured proteins in an ATP-dependent manner. There are two distinct groups of chaperonins: group I chaperonins of eubacteria, mitochondria and chloroplasts, and group II chaperonins of archaea and the eukaryotic cytosol.

Group II chaperonins act independently of a cofactor corresponding to GroES of group I chaperonins. Instead, the helical protrusion at the tip of the apical domain, which forms a built-in lid of the central cavity, is considered to substitute for the cofactor. However, the exact role of the helical protrusion remains unclear. To clarify this issue, we constructed three deletion mutants of α chaperonin from a hyperthermophilic archaeum, *Thermococcus* sp. strain KS-1 (*T.* KS-1), lacking one third, two thirds, and the whole of the helical protrusion, and analyzed their molecular properties.

Three mutants lacking 10, 20 and 32 residues in the helical protrusion (termed αDel I, αDel II, and αDel III) were constructed, and their molecular chaperone activities were examined using citrate synthase and GFP as

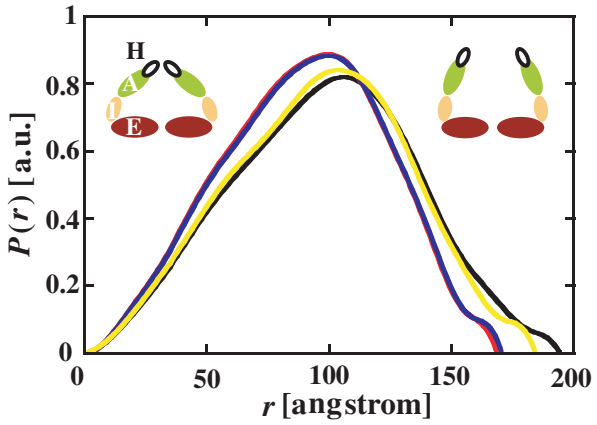

Figure 22
P(*r*) functions of αWT in the absence and presence of adenine nucleotides. *Black line*, without addition of nucleotides; *red line*, incubated with ATP; *blue line*, incubated with AMP-PNP; *yellow line*, incubated with ADP; a.u., arbitrary units. *A*, *I*, and *E* refer to the apical, intermediate, and equatorial domains, respectively. *H* represents the helical protrusion.

substrate proteins. Protease sensitivity assays and small-angle X-ray scattering (SAXS) experiments were conducted to demonstrate the conformation change of the wild type protein (αWT) and deletion mutants by adenine nucleotides. The SAXS experiments were performed at BL-15A. Pair distribution (*P*(r)) functions were calculated by using GNOM software. The values of radius of gyration (R_g) and maximum particle distance (D_{max}) were estimated from the *P*(r) function.

Protease sensitivity assays and the SAXS experiments revealed that ATP induces a drastic conformational change in αWT under potassium-free conditions. The observed difference between the absence and presence of ATP is about 26 Å in terms of the value of D_{max}. AMP-PNP, non-hydrolysable analogue of ATP, induced a similar conformational change in the absence of potassium ion. The ATPase activity of αWT is dependent on potassium ion, and is effectively inhibited by its absence. These results indicate that the hydrolysis of ATP is dispensable for this change. On the contrary, significant structural changes of the deletion mutants were not observed in the presence of ATP or AMP-PNP. These findings clearly demonstrate that the conformational change of αWT induced by ATP binding is a movement of the helical protrusion. From the structural parameters of the model structures, it is considered that the closing of the chaperonin cavity is induced by the binding of ATP (Fig. 22).

Interestingly, we observed that the deletion mutants have no significant ATP-dependent protein folding activity, even though they are capable of binding unfolded proteins. Taken together, we conclude that productive protein folding requires a complete closure of the ring cavity. It is likely that even a partial deletion of the region makes it impossible to seal off the central cavity and encapsulate the bound substrate. As was expected, the helical protrusion of group II chaperonins is likely to play an equivalent role to GroES in group I chaperonins.

R. Iizuka[1], S. So[1], T. Inobe[2, 3], T. Yoshida[1, 4], T. Zako[1, 5], K. Kuwajima[2] and M. Yohda[1] ([1]Tokyo Univ. of Agric. Technol., [2]Univ. of Tokyo, [3]Northwestern Univ., [4]JAMSTEC, [5]RIKEN)

Reference

[1] R. Iizuka, S. So, T. Inobe, T. Yoshida, T. Zako, K. Kuwajima and M. Yohda, *J. Biol. Chem.*, **279** (2004) 18834.

8-11 Solution NMR Structure and X-ray Absorption Analysis of the C-terminal Zinc Binding Domain of the SecA ATPase

SecA is the ATPase subunit of bacterial preprotein translocase. The extreme C-terminus of SecA from *E. coli* harbours a highly conserved Zn^{2+}-binding domain, "SecA-ZBD". This 22 residue sequence, when bound to Zn^{2+}, is important for interactions with the translocation-specific chaperone, SecB, and with acidic phospholipids. A phylogenetic analysis of SecA molecules coded in bacterial genomes indicates that the SecA-ZBD is present in organisms that do not have a gene for SecB, indicating that this domain may have additional functions. The ZBD is attached to the main body of the SecA enzyme by a non-conserved and flexible linker; the linker and ZBD are not present in the crystal structure of SecA from *B. subtilis*, and they must be removed prior to crystallization of *E. coli* SecA. To obtain an atomic-resolution structure for the SecA ZBD, we used a combination of NMR spectroscopy and X-ray scattering.

The sequence of the 22 residue peptide used for these studies was: Ac-KVGRNDPCPCGSGKKYKQCH-GRLQ. We used two-dimensional proton NMR to solve the structure of the SecA-ZBD. From this work, we learned that the Zn^{2+}-bound SecA-ZBD forms a tightly folded and stable structure which is stabilized primarily through peptide-Zn^{2+} interactions, as well as the formation of a small hydrophobic core consisting of Val2 and Tyr16.

The NMR experiments did not provide us with any direct information on the location of the Zn^{2+} ion. We did model a Zn^{2+} ion into the structure, but the coordination geometry and bond distances between Zn^{2+} and the side chains of Cys8, Cys10, Cys19, and His20, appeared to be distorted. To obtain detailed information on the interactions between the Zn^{2+} ion and the peptide, EXAFS experiments were conducted at BL-12C. The absence of a peak at 9663 eV in the XANES spectrum of the SecA-ZBD (Fig. 23(A)) was consistent with 4-coordination of the Zn^{2+} ion. The EXAFS spectrum and corresponding Fourier transform (Fig. 23(B)) were used to model the four Zn^{2+} ligands as three sulphur atoms, with an average Zn^{2+}-S distance of 2.30 Å, and one nitrogen atom at a distance of 2.03 Å. Incorporation of the constraints into our structure calculation allowed us to include the Zn^{2+} atom in the NMR-derived structure (Fig. 24).

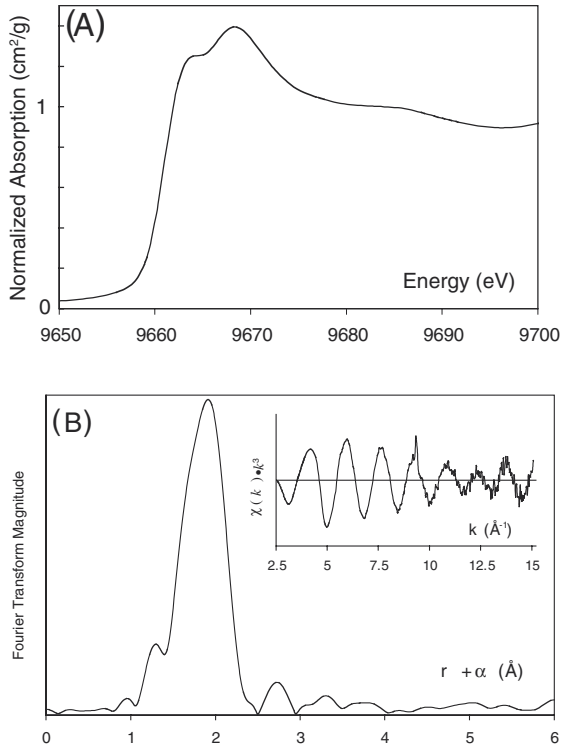

Figure 23
X-ray absorption analysis of the SecA-ZBD. (A) Normalized XANES spectrum (B) k^3-weighted Zn^{2+} K-edge EXAFS spectrum and corresponding Fourier Transform (inset). Reproduced from *Biochemistry* 2004, 43:9361-9371. Copyright 2004 Am. Chem. Soc.

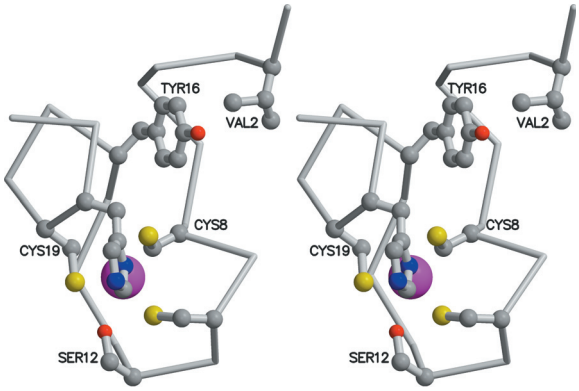

Figure 24
Stereoview of the Structure of the Zn^{2+}-bound SecA-ZBD using combined NMR and EXAFS data. Reproduced from *Biochemistry* 2004, 43:9361-9371. Copyright 2004 Am. Chem. Soc.

Some of the noteworthy features of the structure include the fact that two of the Zn^{2+} ligands, Cys19 and His20, are adjacent to each other. This is extremely uncommon for Zn^{2+} binding proteins, probably because of the relatively high energy required for proper positioning of the two side chains. In fact, Cys19 is the only residue in the structure whose main chain conformation falls in a disallowed region of the Ramachandran plot ($\phi = -150°$, $\psi = -79°$). Another interesting feature is the presence of Ser12 which makes important "second sphere" interactions with the Zn^{2+}-binding residues. Ser12 is strictly conserved among all known SecA-ZBD sequences, and our NMR data show that the Oγ proton is in slow exchange with solvent, and there are NOEs present between this proton and a number of other protons in its vicinity. Ser12 appears to be important because it makes a very strong hydrogen bond with Cys19.

This type of Zn^{2+} binding motif is not present in the genomes of eukaryotes; however, it is present in a number of proteins of unknown function from prokaryotes. We are investigating whether these proteins are involved in secretion, or if they have an unrelated function.

B. Dempsey[1], F. Jalilehvand[2], G. S. Shaw[1], and B. Shilton[1] ([1]Univ. of Western Ontario, [2]Univ. of Calgary)

References

[1] B. R. Dempsey, M. Wrona, J. M. Moulin, G. B. Gloor, F. Jalilehvand, G. Lajoie, G. S. Shaw and B. H. Shilton, *Biochemistry*, **43** (2004) 9361.

8-12 Observation of Microbeam-irradiated Sites in Mammalian Cell Nuclei

In order to study the radiobiological effects by low dose radiation, a cell irradiation system using synchrotron X-ray microbeam has been developed, by which we can irradiate and observe irradiated and non-irradiated cells individually. Using this system, we can also study "bystander effects", the radiation-induced effects observed in cells which have not accepted any tracks of radiation, but been situated around the cell actually irradiated.

Developed system is composed of three parts. The first part is to produce X-ray microbeam, either by a Kirkpatrick Baez (K-B) mirror system to focus the X-ray beam or a high-precision slit system to cut out the beam. Then, the beam is reflected right angle upward by diffraction of Si(311). The second is an epi-fluorescent microscope equipped with a precise motorized stage, on which the sample dish is fixed and irradiated with X-ray microbeam. The third is a fluorescence image analyzer (computer) with a sensitive CCD camera, which recognizes the target cells and their positions. It also controls irradiation of X-ray beam to the target cells, one by one, automatically. This system has been installed at BL-27B. Experimental stations at BL-27 are situated in the biological sample preparation area, where incubators and other equipments to grow and handle mammalian cells are available. Minimum beam sizes obtained so far are 2 μm in diameter by the K-B mirror system, and 5 μm square by the slit system. This system can irradiate several hundreds of cells per hour, fast enough to irradiate the cells in a good physiological condition.

Fig. 25 demonstrates the performance of the system. Sample cells (human fibroblast, NB1-RGB) in a dish were irradiated with the microbeam, and the irradiated cells were observed after the immunostaining treatment in the biological laboratory. Phosphorylated histone H2AX (called γ-H2AX), which is known to appear after

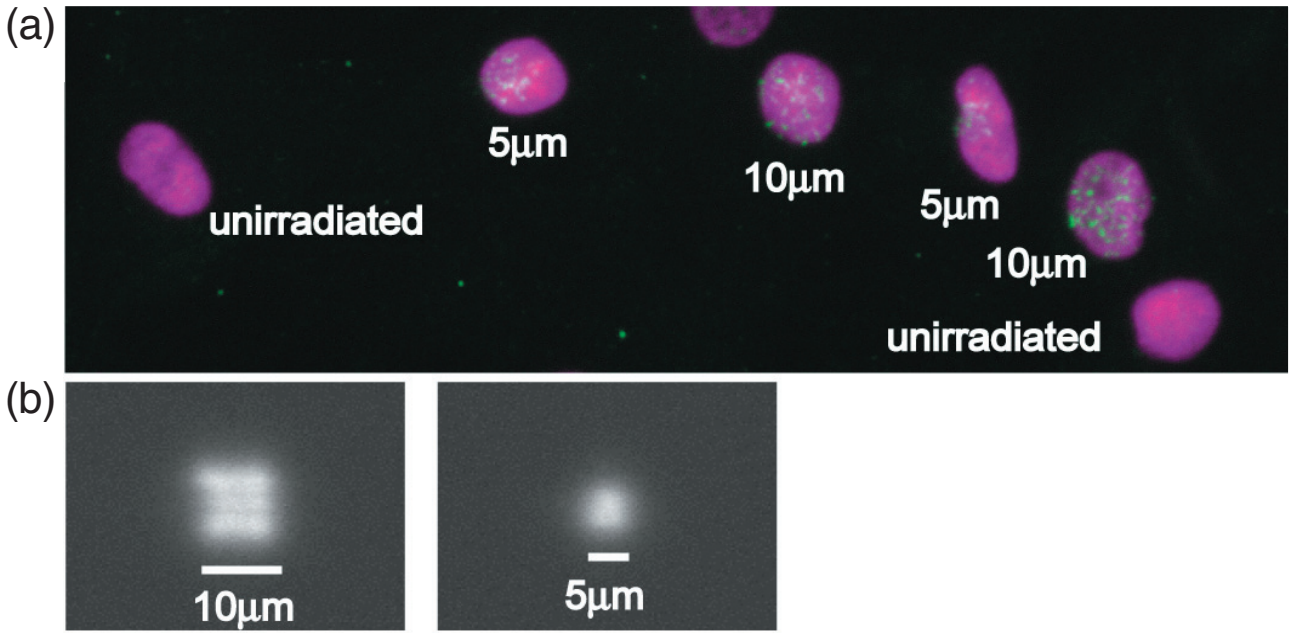

Figure 25
(a), Fluorescent image of human fibroblast cells. All the cell nuclei were stained with propydium iodide (PI) and appeared in purple. Phospholyrated histone H2AX (γ-H2AX), induced as the result of the production of DNA double strand breaks by X-rays, were observed in green by staining with the two-step immunostaining of γ-H2AX.
(b), Images of the X-ray microbeam of 10 μm square and of 5 μm square, visualized by scintilater set on the sample dish. Magnification scale is the same with panel (a).

the induction of DNA double strand breaks, can be microscopically visualized with a γ-H2AX antibody as foci in cell nuclei. Since the slit system installed in the system enables to change the size of the beam easily (the minimum size, 5 μm square), we irradiated the cells with two different beam-size, either 5- or 10-μm square, as shown in the figure. All the irradiated cells could be observed at the revisited position, and could be distinguished from surrounding unirradiated cells by their high yield of fluorescence of γ-H2AX. Most of the fluorescent foci were observed in localized area in cell nuclei, the size of which was almost the same as the beam size. Difference in size of the stained area can be easily recognized when compared between cells irradiated 5-μm beam and those irradiated with 10-μm beam. Dose dependence of γ-H2AX induction was also clearly observed. Survival study, which needs to irradiate many cells individually and sequentially with the microbeam, has also been done. The result clearly indicates that the cell nucleus is the target organelle which is responsible for the cell killing effect. These results demonstrate that the system has achieved the specifications as designed.

N. Usami and K. Kobayashi (KEK-PF)